# Ice Crystal Drag Model Extension to Snowflakes: Experimental and Numerical Investigations

Boris Aguilar, Pierre Trontin, Louis Reitter, Kilian Köbschall, Fabien Dezitter, Ilia Roisman, Philippe Villedieu

▶ **To cite this version:**

Boris Aguilar, Pierre Trontin, Louis Reitter, Kilian Köbschall, Fabien Dezitter, et al.. Ice Crystal Drag Model Extension to Snowflakes: Experimental and Numerical Investigations. AIAA Journal, In press, pp.1-14. 10.2514/1.J062122 . hal-03774518

**HAL Id: hal-03774518**
**https://hal.science/hal-03774518**

Submitted on 10 Sep 2022

**HAL** is a multi-disciplinary open access archive for the deposit and dissemination of scientific research documents, whether they are published or not. The documents may come from teaching and research institutions in France or abroad, or from public or private research centers.

L'archive ouverte pluridisciplinaire **HAL**, est destinée au dépôt et à la diffusion de documents scientifiques de niveau recherche, publiés ou non, émanant des établissements d'enseignement et de recherche français ou étrangers, des laboratoires publics ou privés.

# Ice crystal drag model extension to snowflakes: experimental and numerical investigations.

Boris Aguilar*
*Airbus Helicopters S.A.S., 13725 Marignane, France*
*ONERA, 31055 Toulouse, France*

Pierre Trontin†
*University of Lyon, 69622 Villeurbanne, France*

Louis Reitter and Kilian Köbschall‡
*T.U. Darmstadt, 64287 Darmstadt, Germany*

Fabien Dezitter§
*Airbus Helicopters S.A.S., 13725 Marignane, France*

Ilia Roisman¶
*T.U. Darmstadt, 64287 Darmstadt, Germany*

Philippe Villedieu‖
*ONERA, 31055, Toulouse, France*

**To ensure safe flight under snowy conditions, aircraft manufacturers must demonstrate that each engine and its air inlet system can operate throughout the flight power range of the engine (including idling) in both falling and blowing snow conditions. This study is part of an effort to develop models for snow accretion. The focus here is on the modeling of snowflake transport by the carrier airflow and more specifically on the modeling of the drag coefficient of snowflakes. Based on comparisons between numerical and experimental results, we show that, provided that the complex shape of the snowflakes is accounted for, the models initially developed for ice crystal icing can also be used to estimate the drag coefficient of a snowflake. We also propose a methodology to estimate the geometric parameters of the drag models from 2D images of the particles which in general are the only available experimental data.**

## Nomenclature

*PhD student
†Professor, Univ Lyon, Univ Claude Bernard Lyon 1, CNRS, Ecole Centrale de Lyon, INSA Lyon, LMFA, UMR5509. Corresponding author, pierre.trontin@univ-lyon1.fr.
‡PhD students, Institute for Fluid Mechanics and Aerodynamics.
§Icing expert
¶Professor, Institute for Fluid Mechanics and Aerodynamics.
‖Research Director, DMPE, University of Toulouse.
Presented as Paper 2021-2684 at the AIAA Aviation 2021 Forum, virtual event, August 2-6, 2021

| | | |
|---|---|---|
| $m_p$ | = | Particle mass |
| $\boldsymbol{v_p}$ | = | Particle velocity |
| $\boldsymbol{v_a}$ | = | Air velocity |
| $\boldsymbol{w}$ | = | Relative velocity between air and particle |
| $f_{max}$ | = | Maximum diameter of Feret |
| $f_{max}^{\perp}$ | = | Maximum crosswise diameter of Feret |
| $A^{\perp}$ | = | Particle shadow area |
| $V_{spheroid}$ | = | Volume of the reconstructed spheroid |
| $A_{spheroid}$ | = | Surface of the reconstructed spheroid |
| $d_V$ | = | Particle volume equivalent diameter |
| $d_m$ | = | Particle mass equivalent diameter |
| $\Phi$ | = | Particle sphericity |
| $\Phi^{\perp}$ | = | Particle crosswise sphericity |
| $\boldsymbol{F_D}$ | = | Drag force |
| $\boldsymbol{g}$ | = | Gravity |
| $\rho_a$ | = | Air density |
| $A_{ref}$ | = | Particle reference surface associated to the drag coefficient in the drag force definition. |
| $d_{ref}$ | = | Particle characteristic length scale |
| $C_D$ | = | Drag coefficient |
| $Re_p$ | = | Particle Reynolds number |
| $\rho_p$ | = | Particle density |
| $\rho_w$ | = | Water density |
| $\mu_a$ | = | Air dynamic viscosity |
| $A_r$ | = | Area ratio |
| $x_{px}$ | = | Width of one pixel |
| PIP | = | Precipitation Imaging Probe |

## Introduction

To ensure safe flight under snowy conditions, aircraft manufacturers must demonstrate that each engine and its air inlet system can operate throughout the flight power range of the engine (including idling) in both falling and blowing snow conditions, without adverse effect on engine operation (power or thrust loss, surge, stall or flameout).

Snow particles are precipitation sized ice particles that form in clouds and precipitate to the ground. Falling snow

formation has its origin in a complex interplay of microphysical processes (vapor deposition, riming and aggregation, fall of the hydrometeors at different speeds depending on their size and shape), which are governed by cloud dynamics (vertical and horizontal transport) and thermodynamics (temperature and humidity vertical profiles). Snow particles have interested scientists since a long time and the first systematic studies of snow crystals started with the pioneering work of Nakaya [1]. Numerous studies about snow particles have been published in contemporary literature since these early studies. In particular, in the framework of meteorological applications, the works of [2–7], dedicated to the prediction of the terminal velocity of naturally falling snowflakes, can be mentioned. The terminology of Pruppacher and Klett [8] is adopted here: ice particles grown by vapor deposition and/or riming are called *snow crystals* and aggregates of snow crystals are referred to as *snowflakes*.

Due to the variability of atmospheric conditions prevailing in snow clouds, the shape, size, density, and related properties such as drag and terminal fall speed of natural snow particles (snow crystal and snowflakes) are found to be highly variable. Regarding the shape for instance, Fig. 1 presents samples of ice crystals (columns, columns with plates, plates in the top row, planar dendrites in the third row, graupel or snow pellets in the fifth row) and snowflakes with different degrees of riming in the three last rows.

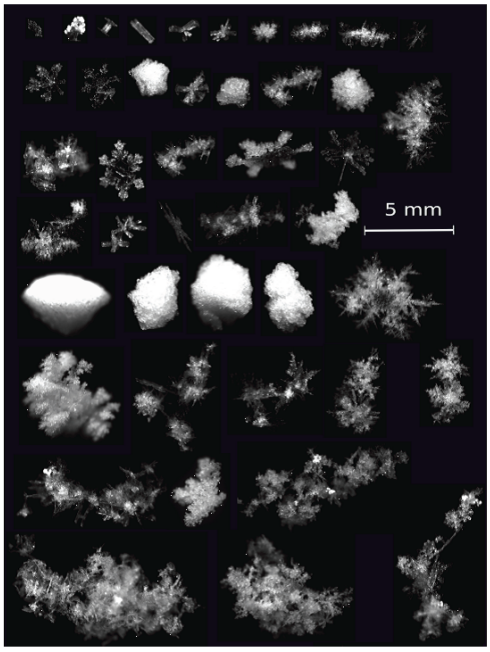


**Fig. 1 MASC picture of hydrometeor illustrating the variability in the shape and size of snow particles. Reprinted with permission from [9]. Copyright 2012 authors (distributed under the Creative Commons Attribution 3.0 License).**

In a context where aircraft manufacturers must comply with certifications requirements to ensure safe aircraft operation in snowy conditions, models and numerical simulation methodologies are an important asset to limit costly icing wind tunnel and flight tests. The main objective of this paper is to propose models for the transport of snowflakes by

the airflow, which is a first step in the computation of snow accretion on an aeronautical surface. This paper focuses on the trajectory of snowflakes, including the evaluation of the drag coefficient. Thermal aspects, in particular the melting of particles during transport, will be addressed in a future paper. In the particular case of snow, the main difficulty consists in developing models that take into account the geometrical complexity of the particle from experimental data that are often partial and that do not allow the complete geometrical characterization of the snowflake. This is the case when using a Precipitation Imaging Probe (PIP) from Droplet Measurement Technologies to characterize the geometry of snowflakes during a flight test campaign. Figure 2 shows the installation of the PIP among two other probes, the Cloud Imaging probe (CIP) and the High Speed Imager (HSI) on the left wing of an ATR 42. Only PIP and CIP probes were used for the ICEGENESIS [10] flight test campaign, as the HSI probe was ultimately not installed. The operating

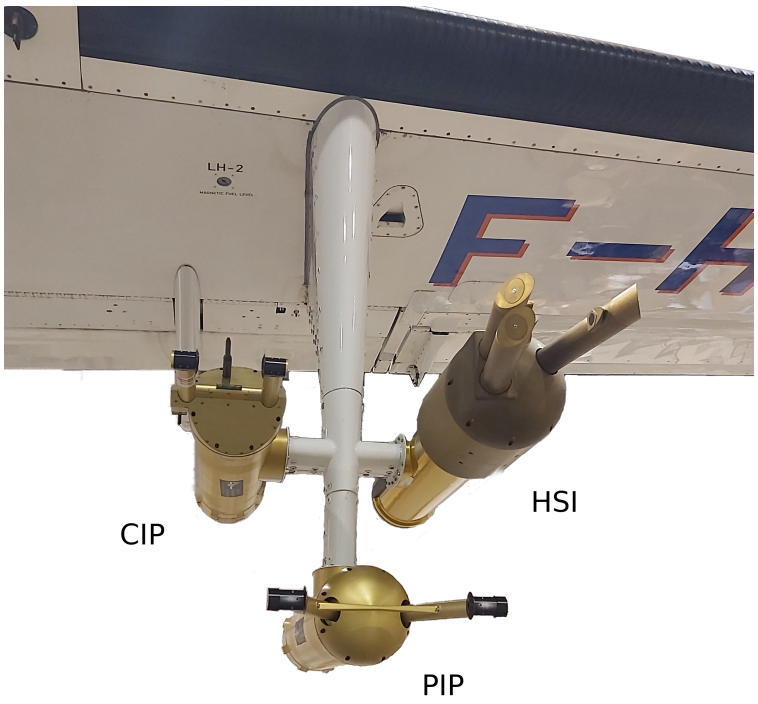


**Fig. 2 CIP, HSI and PIP probes installed on the left wing of the ATR 42 managed by SAFIRE, the French facility for airborne research.**

principle of the PIP is illustrated in Fig. 3. It is an imager used to measure the snowflake shape from shadow images of particles passing through a collimated laser beam that are projected onto a linear array of 64 photodetectors. Particle images are reconstructed from individual 1D slices, each slice corresponding to the part of the particle illuminated by the laser beam at a given time (Figs. 3c and 3d). The snowflake is then represented by a single projected 2D image (Figs. 3e and 3f), which limits the geometric description of the whole particle. The post-processed image obtained depends on the position of the PIP sensors with respect to the orientation of the particle. This is illustrated in Fig. 3 where the

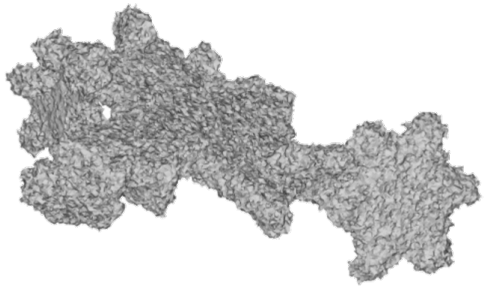

(a) Snowflake view #1.

(b) Snowflake view #2.

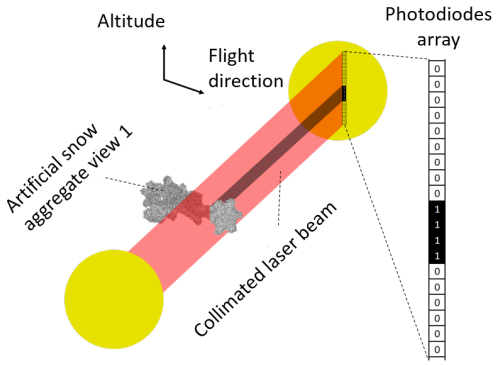


(c) Image acquisition from PIP (view #1).

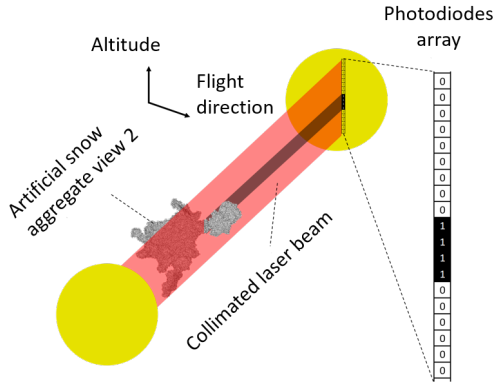


(d) Image acquisition from PIP (view #2).

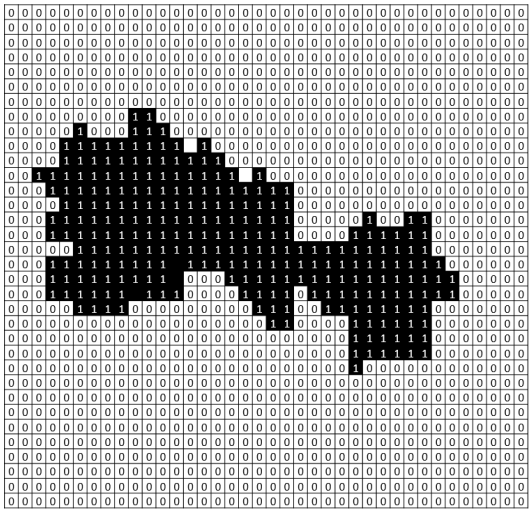

(e) Post processed image (view #1).

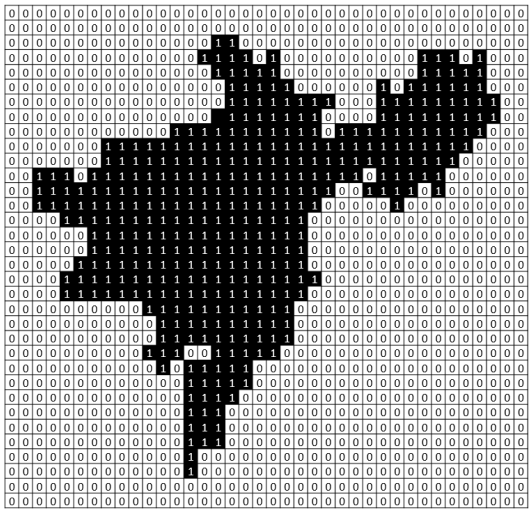

(f) Post processed image (view #2).

**Fig. 3 Snowflake post processed image from PIP. Left: view #1. Right: view #2.**

same snowflake is shown from two different orientations (Fig. 3a for view #1 and Fig. 3b for view #2) resulting in two different 2D images from the PIP. In addition, from the point of view of drag force calculation, the position of the PIP sensor relative to the particle is not necessarily the most relevant since the measured projected area should normally correspond to the cross section of the particle normal to the flow. Furthermore, the characterization of the snowflake shape by a single image does not account for the anisotropy of the particle.

The variability in particle shape and bulk density was not addressed by the European projects HAIC [11] and MUSIC-haic [12], where models for trajectory, impact and erosion [13–29] were derived for ice particles (referred to as *ice crystals* in the rest of the manuscript) with high bulk densities (typically of the order of 917 kg.m$^{-3}$) and fairly regular geometric shapes (sphericities larger than 0.8). Regarding the specific risk of snow accretion or accumulation, there are currently no validated engineering tools (test facilities and numerical tools) available for snowflakes. The extension and validation of the models from ice crystal icing to snowy conditions is the main objective of this paper. More specifically the focus is on the modeling of the drag coefficient of snowflakes. The influence of the accuracy of the input data for the models will be studied. To this end, emphasis will be placed on the geometric procedure which is used to reconstruct a simplified 3D shape of the particle from a single post-processed PIP image (typical data format from a flight test campaign). This work is thus part of an effort to meet the requirements of the aeronautical community, namely to propose models whose input data are compatible with those from wind tunnels and flight tests.

The rest of the paper is divided in four parts followed by some conclusions. In a first part, the experiments dedicated to the measurement of the drag coefficient of a free falling snowflake are described. The procedure for post-processing images generated by the experiments and allowing a 2D to 3D geometric reconstruction is also described. The second part presents the extension of the drag models for ice crystals to the case of snowflakes and the third part is dedicated to the comparison between model predictions and experimental results. A fourth part is dedicated to discussion.

## I. Experiments: free fall of a snowflake

### A. Experimental Apparatus

For the experiments, artificial snowflakes are used, generated using the SnowFALL device provided by the company IAG. These snowflakes have an irregular shape, close to natural snowflakes like those depicted in Fig. 1. The experimental setup used for the measurement of snowflake drag is schematically shown in Fig. 4. The entire setup and measurement equipment is mobile and can be operated at ambient temperatures down to −20 °C. The setup consists of a large PMMA tube with a diameter and height of 150 mm and 300 mm, respectively. Through a baffle (opening of 10 mm) at its top, free falling snowflakes enter the PMMA tube, which has the purpose of shielding them from possible external gusts influencing their trajectory. Immediately after a snowflake falls out of the PMMA tube, its movement is captured using high-speed cameras in a front, side and bottom view using a recording speed of 3000 frames

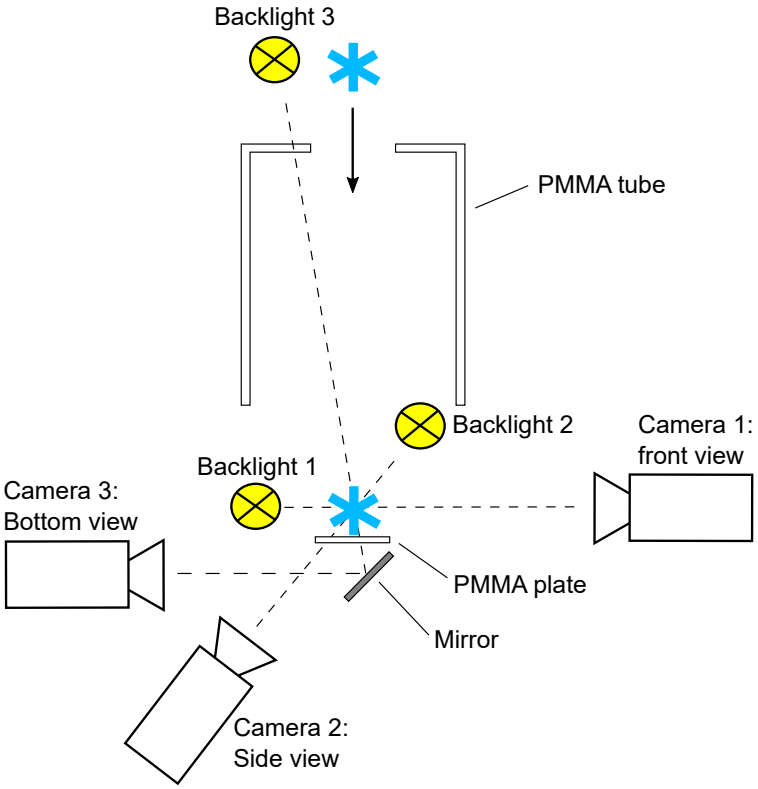


**Fig. 4 Schematic view of the experimental setup used to measure snowflake drag.**

per second. The resolutions of the front, bottom and side views are 24.1 µm/pixel , 34.6 µm/pixel and 51.7 µm/pixel, respectively. The side view has the largest field of view and is primarily used for measuring the free fall velocity. After the measurement of their terminal velocity, the snowflakes are caught and melted on a transparent, superhydrophobic coated PMMA plate, forming nearly spherical liquid drops. These drops are captured using the front view camera, which allows measurement of the drop diameter and therefore, the computation of the snowflake mass. Measurement of the snowflake projected area in three nearly orthogonal views, as well as measuring their mass, allows the calculation of the snowflake drag coefficient corresponding to its characteristic terminal velocity. Figure 5 shows example images of a snowflake in the front view, falling with a terminal velocity of 1.36 m/s and finally landing on the PMMA plate. The snowflake's maximum dimension is 3.5 mm. As shown in Fig. 5, a snowflake might be very fragile and shatter when it impinge the PMMA plate, even if it falls with a rather moderate terminal velocity. In the case of fragmentation, all fragments are collected and melted together, using a stream of hot air directed toward the bottom of the PMMA plate. As a result, an almost spherical drop is formed on top of the superhydrophobic PMMA plate, an example which can be seen in Fig. 6. It can be observed that the droplet surface is flat at its contact with the PMMA plate. Given that the drop can be depicted as a body of revolution, its geometry can be defined using only a single image in which the drop symmetry axis is aligned with the camera focal plane. The symmetry axis of the drop is assumed to be aligned normal to the PMMA surface, intersecting with the drop centroid and the distance of each pixel inside the drop to this axis in

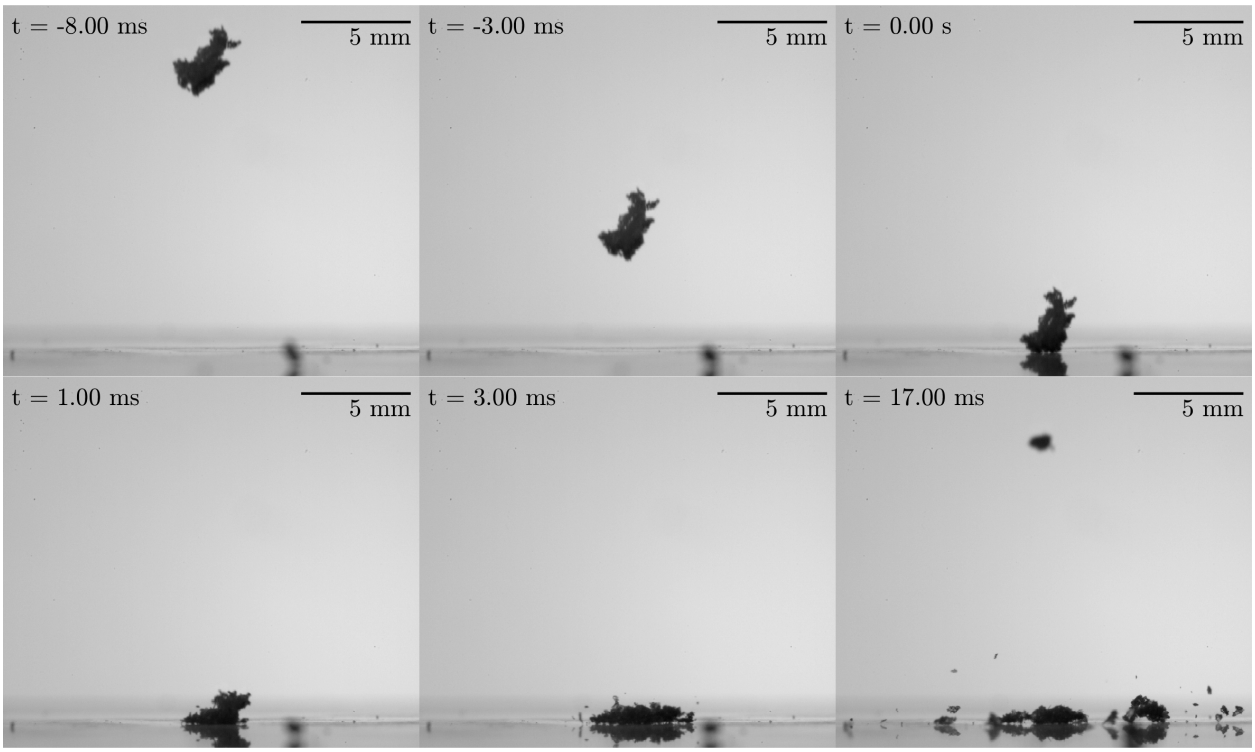


**Fig. 5 Example images of a snowflake recorded with camera 1 (front view) having a resolution of 24.1 µm/pixel.**

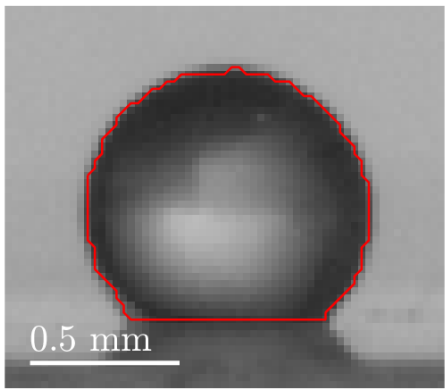


**Fig. 6 Image of the melted snowflake, having a mass of 0.263 mg and a diameter of 0.795 mm.**

meters, $r_j$, is determined. Then, the drop mass can be computed as:

$$m_p = \rho_w \sum_{j=1}^{N} \frac{\pi x_{px}}{2} \Big[ (r_j + x_{px}/2)^2 - (r_j - x_{px}/2)^2 \Big], \tag{1}$$

where $\rho_w$ is the water density, $x_{px}$ is the width of one pixel in meters and N is the number of all pixels located inside of the drop. The diameter of the drop is approximately 0.8 mm and its mass is computed as 0.263 mg. Using the snowflake

images of the front, side and bottom view, characteristic size and shape parameters can be derived. Unlike a PIP where only a single image is available, the three views obtained from the three high-speed cameras will allow to evaluate the sensitivity of the computed terminal falling velocity with respect to the position of the camera used for the 2D to 3D geometric reconstruction of the particle (see Sec. I.B).

### B. Image post-processing

In this part we briefly present the post-processing procedure of the images acquired during the experiments described in the previous section. The technique described here is the one that would be also used to process PIP images. Umbroscopic measurements provide grayscale or black and white images of the snowflake shadow area in the direction of the camera (Fig. 7a). A preliminary step of digitizing the grayscale image is performed. For each pixel of the image,

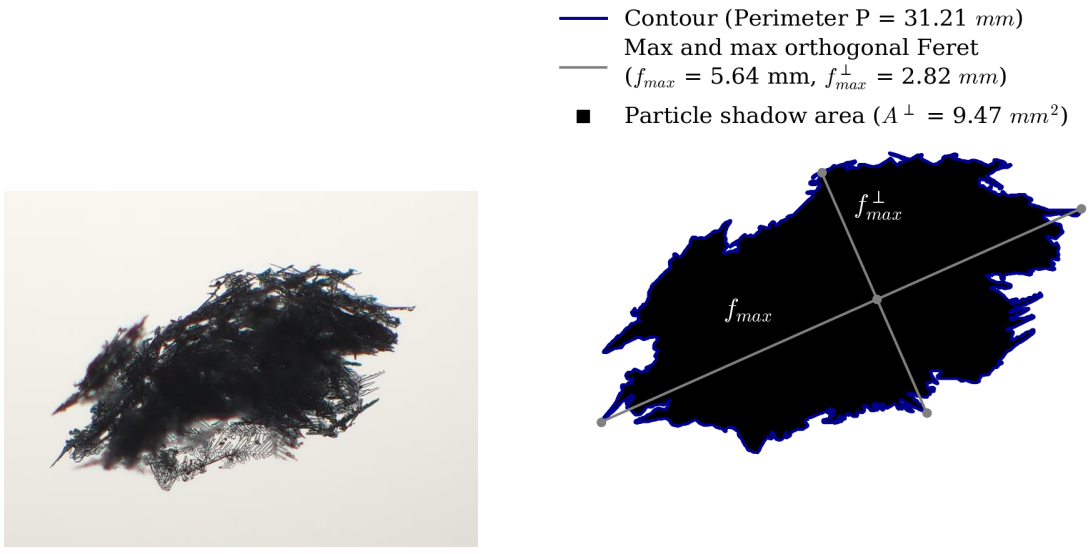


(a) Grayscale image of a snowflake.

(b) Post processed image.

**Fig. 7 Data post-processing illustration.**

if the gray level is higher than that of the background of the image, the value of the pixel is imposed to 1. Otherwise, the value of the pixel is imposed to 0. An automatic image post-processing tool has been developed to provide the maximum $f_{max}$ and maximum crosswise $f^{\perp}_{max}$ diameters of Feret (in gray in Fig. 7b) from the digitized image. Reconstructed snowflake shadow area $A^{\perp}$ is also derived (in black in Fig. 7b). $f^{\perp}_{max}$ is defined as the largest diameter among all diameters orthogonal to $f_{max}$. Using Feret's diameters, it can be deduced an ellipse of major semi axis $a = f_{max}/2$ and minor semi axis $c = f^{\perp}_{max}/2$ (in gray in Fig. 8). From the axes of the ellipse it can be constructed either an oblate spheroid (generated by rotation of the ellipse around its $z$ minor axis, Fig. 8a) or a prolate spheroid (generated by rotation of the ellipse around its $y$ major axis, Fig. 8b) of volume $V_{spheroid} = \pi/6A^2C$. For an oblate spheroid $A = 2a$

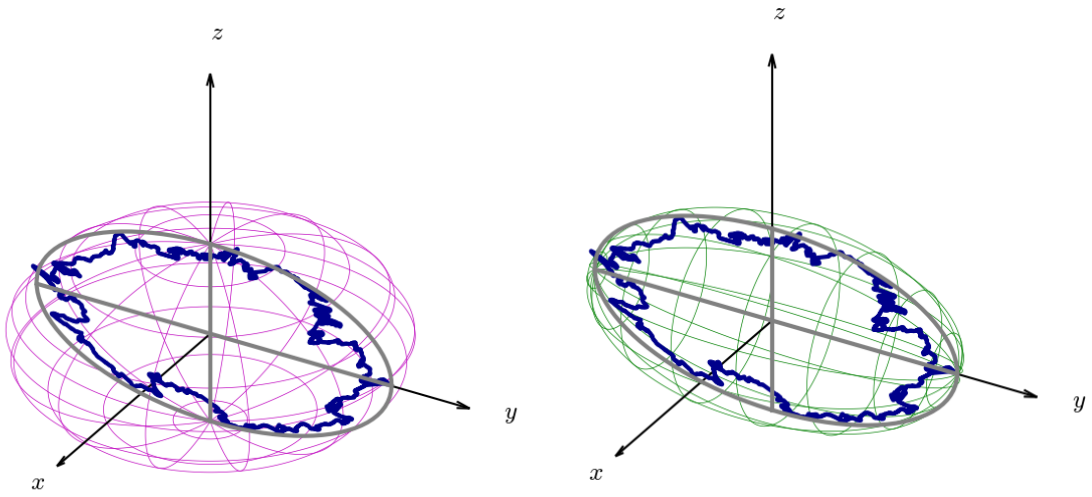


(a) Oblate spheroid reconstruction.

(b) Prolate spheroid reconstruction.

**Fig. 8 Oblate and prolate spheroid reconstructions.**

and $C = 2c$, while for a prolate spheroid $A = 2c$ and $C = 2a$. Using these parameters, the following characteristics can be deduced:

$$d_V = \left(\frac{6V_{spheroid}}{\pi}\right)^{1/3}, \quad \Phi = \frac{\pi d_V^2}{A_{spheroid}}, \quad \Phi^{\perp} = \frac{\frac{\pi}{4} d_V^2}{A^{\perp}} \tag{2}$$

where $d_V$ is the volume equivalent diameter, $A^{\perp}$ the snowflake shadow area (Fig. 7b) and $A_{spheroid}$ is the surface of the spheroid. $A_{spheroid} = 2\pi a^2 + \pi \frac{c^2}{e} \ln\left(\frac{1+e}{1-e}\right)$ for an oblate spheroid and $A_{spheroid} = 2\pi a^2 \left(1 + \frac{c}{ae} \arcsin e\right)$ for a prolate spheroid. $\Phi$ and $\Phi^{\perp}$ are respectively the particle sphericity and crosswise sphericity. The eccentricity of the ellipse is defined as $e = \sqrt{1 - \frac{c^2}{a^2}}$.

## II. Models for snowflake trajectory

For the computation of snow particle trajectory, only the drag force is considered in the momentum equation, and the influences of the added mass force, the Basset force, and the lift force are neglected. Regarding the added mass and Basset forces, this is justified because the density of the air is much lower than the bulk density of a snowflake. Concerning the lift force, this comes from the fact that a snowflake rotates on itself during its motion so that the average value (but not the instantaneous value) of the lift force can be considered as zero. Hence, the particle motion equation simply reads:

$$m_p \frac{\mathrm{d}\boldsymbol{v_p}}{\mathrm{d}t} = \boldsymbol{F_D} + m_p \boldsymbol{g}, \quad \boldsymbol{F_D} = -\frac{1}{2}\rho_a ||\boldsymbol{w}|| \boldsymbol{w} A_{ref} C_D(Re_p) \tag{3}$$

where $m_p$ is the snow particle mass, $\boldsymbol{F_D}$ the drag force, $\boldsymbol{g}$ the gravity, $\rho_a$ the air density and $\boldsymbol{w} = \boldsymbol{v_p} - \boldsymbol{v_a}$ the relative velocity between the air ($\boldsymbol{v_a}$) and the particle ($\boldsymbol{v_p}$). In the following, $||\boldsymbol{w}||$ will simply be denoted $w$. The drag coefficient

$C_D$ is defined with respect to the reference surface $A_{ref}$. It is a function of the particle Reynolds number $Re_p = \frac{\rho_a w d_{ref}}{\mu_a}$ where $\mu_a$ is the air dynamic viscosity, $d_{ref}$ a characteristic length scale and $\rho_a$ the air density. Note that in the present study the mass of the particle $m_p$ is known experimentally. For free fall conditions, the airflow being at rest, the stationary final particle velocity $v_{p_\infty}$ is the solution of Eq. (3) for which the left-hand term has been cancelled:

$$v_{p_\infty} = \sqrt{\frac{2m_p g}{\rho_a A_{ref} C_D(Re_p)}} \tag{4}$$

At steady state, the particle Reynolds number $Re_p$ being itself a function of $v_{p_\infty}$, Eq. (4) is an implicit equation of the unknown $v_{p_\infty}$ which is solved numerically by a Newton algorithm. Note that, according to Eq. (4), if the mass of the particle is known (which is the case here), the velocity $v_{p_\infty}$ is a function of the only product $A_{ref} \cdot C_D$. The models described in the rest of the manuscript will assign different weights to the two contributions $A_{ref}$ and $C_D$.

From a single post processed image of the snowflake (obtained for instance from the PIP), two sets of definitions will be compared to define $d_{ref}$ (as a parameter of $Re_p$), $A_{ref}$ and $C_D$. The first one, based only on a surface description of the particle, is the underlying assumption of models denoted as *surface-based geometric models* in the rest of the manuscript. This is the assumption made by the historical Heymsfield and Westbrook model for snowflakes [2] for which a short description is proposed in Sec. II.A. This model will be the baseline for evaluating the drag coefficient of complex-shaped snow particles. The second one is based on a volume description of the particle, leading to *volume-based geometric models* according to the denomination used in the rest of the paper. This is achieved by introducing the diameters $d_V$ and $d_m$, defining respectively the volume and mass equivalent diameters corresponding to the diameter of the equivalent spherical particle having the same volume (resp. mass) as the snowflake. This is the approach adopted by the Haider *et al.* [30], Ganser [31] and Hölzer *et al.* [32] correlations for non-spherical particles and which has already been validated for ice crystal icing [20, 29]. The extension of these last three models to snowflakes is proposed in Sec. II.B.

### A. Surface-based geometric model for $C_D$: the Heymsfield and Westbrook (H&W) approach

The Heymsfield and Westbrook model [2] is an improvement of the models based on the Abraham's drag coefficient of a sphere [33].

#### *1. The Abraham model for spherical particles*

In Abraham [33], the problem is considered as an assembly of a smooth sphere of radius $a$ plus a thin boundary layer of thickness $\delta$ in a moving fluid of density $\rho_a$ at a velocity $v$. The assembly is then assumed to evolve in an asymptotic low viscosity aerodynamic flow in a regime where the drag coefficient is independant of $Re_p$. These assumptions lead

to the following expression for the drag force of a sphere of radius $a + \delta$:

$$F_D = \frac{\rho_a v^2}{2} \pi (a + \delta)^2 C_{D_0} \tag{5}$$

where $C_{D_0}$ is a constant parameter to be adjusted. Equation (5) may be re-written as:

$$F_D = \frac{\rho_a v^2}{2} \pi a^2 C_{D_0} \left(1 + \frac{\delta}{a}\right)^2 \tag{6}$$

which is the drag force for a particle of radius $a$ with $C_{D_0} \left(1 + \frac{\delta}{a}\right)^2$ as drag coefficient. The boundary layer thickness is given by $\frac{\delta}{a} = \frac{\delta_0}{\sqrt{Re_p}}$ where $\delta_0$ is a dimensionless coefficient. This leads to the following drag coefficient definition for the particle:

$$C_D = C_{D_0} \left[1 + \frac{\delta_0}{\sqrt{Re_p}}\right]^2 \tag{7}$$

where $C_{D_0}$ and $\delta_0$ are chosen to ensure $C_{D_0} \delta_0^2 = 24$ (Stokes regime) and $\delta_0 = 9.06$.

*2. Extension to non-spherical particles*

Many authors have used Eq. (7) for non-spherical particles with $C_{D_0} = 0.35$ and $\delta_0 = 8$. In the definition of $Re_p$, the diameter $d_{ref}$ is then chosen as:

$$d_{ref} = f_{max} \tag{8}$$

where $f_{max}$ is the maximum Feret diameter (Fig. 7b). The reference surface $A_{ref}$ is given by:

$$A_{ref} = A^{\perp} \tag{9}$$

Mitchell, Heymsfield, Khvorostyanov and Curry (MHKC) [3–7] used this method to calculate the drag coefficient and compared the resulting fall velocities for a wide range of particles. Planar and columnar-type, graupel and aggregates with a size range from 250 µm to 8 mm were studied. More recently, Heymsfield and Westbrook found that fall velocities were overestimated for particles with a low area ratio. In some cases the relative error exceeded 100 % and this effect appears to be stronger at low Reynolds number. Needles, dendrites, stellars and aggregates are key particle types that are affected by this bias. To mitigate this high sensitivity to the area ratio, they considered the following modified drag coefficient [2]:

$$C_D^* = C_D A_r^{1/2} \tag{10}$$

where $A_r$ is the area ratio defined by:

$$A_r = \frac{A^{\perp}}{\pi f_{max}^2 / 4} \tag{11}$$

Provided that $m_p$ is known (which is the case here), all necessary geometric information for the computation of the drag coefficient $C_D$ is extracted from the 2D image ($f_{max}$ and $A^{\perp}$).

### B. Volume-based geometric models for $C_D$: the Haider *et al.*, Ganser and Hölzer *et al.* approaches

Among all the general mathematical expressions that can be found in the literature for the drag coefficient of non-spherical particles, we can mention the models of Haider & Levenspiel (H&L) [30], Ganser (Ga) [31] and Hölzer & Sommerfeld (H&S) [32]. for which the drag coefficients, respectively denoted as $C_D^{H\&L}$, $C_D^{Ga}$ and $C_D^{H\&S}$, can be written as a function of $Re_p$, $\Phi$ and $\Phi^{\perp}$ as follows (see [30–32] for a complete description and the appendix for a summary of the models):

$$C_D^{H\&L} = C_D^{H\&L}\left(Re_p, \Phi\right) \tag{12a}$$

$$C_D^{Ga} = C_D^{Ga}\left(Re_p, \Phi, \Phi^{\perp}\right) \tag{12b}$$

$$C_D^{H\&S} = C_D^{H\&S}\left(Re_p, \Phi, \Phi^{\perp}\right) \tag{12c}$$

For the three models H&L, Ga and H&S, several definitions are possible for $d_{ref}$. These will be given below. From $d_{ref}$, the reference surface is defined as:

$$A_{ref} = \pi d_{ref}^2/4 \tag{13}$$

while the particle Reynolds number is given by:

$$Re_p = \frac{\rho_a w d_{ref}}{\mu_a} \tag{14}$$

The main point is the definition of the particle reference diameter $d_{ref}$. Two approaches will be compared to define it, namely an *ice-core density-based* approach and an *ice-bulk density-based* approach .

#### *1. Ice-core density-based approach*

This is the approach proposed in the framework of ice crystal icing [20, 29] where ice crystals are assumed to be compact with a density close to the ice core density $\rho_i^{\text{core}}$:

$$\rho_p = \rho_i^{\text{core}} \tag{15}$$

where $\rho_i^{\text{core}} = 917\,\text{kg.m}^{-3}$. The reference diameter $d_{ref}$ is then defined as the mass equivalent diameter $d_m$ corresponding to the diameter of the equivalent spherical particle of density $\rho_i^{\text{core}}$ having the same mass $m_p$ as the snowflake:

$$d_{ref} = d_m = \left(\frac{6m_p}{\pi\rho_i^{\text{core}}}\right)^{1/3} \tag{16}$$

The volume of the equivalent spherical particle is given by $m_p/\rho_i^{\text{core}}$. The values of $\Phi$ and $\Phi^{\perp}$ are respectively defined in this case as:

$$\Phi = \frac{\pi d_m^2}{A_p} \tag{17a}$$

$$\Phi^{\perp} = \frac{(\pi/4)\, d_m^2}{A^{\perp flow}} \tag{17b}$$

where $A_p$ is the surface of the snowflake and $A^{\perp flow}$ its projected surface normal to the airflow. Note that $A_p$ and $A^{\perp flow}$ are not known a priori.

In the spirit of the models derived for ice crystal icing [20, 29], the ice-core density-based approach is constructed from the single hypothesis $\rho_p = \rho_i^{\text{core}}$. This approach is therefore suitable when the other geometric parameters $d_m$ (or equivalently $m_p$, Eq. (16)), $\Phi$ and $\Phi^{\perp}$ describing the snowflake are provided experimentally by respectively particle mass, sphericity and orthogonal sphericity distributions representing the variety of snowflakes encountered in the clouds.

*2. Ice-bulk density-based approach*

The reference diameter $d_{ref}$ is defined as the volume equivalent diameter $d_V$ corresponding to the diameter of the equivalent spherical particle having the same volume $V_p$ as the snowflake:

$$d_{ref} = d_V = \left(\frac{6V_p}{\pi}\right)^{1/3} \tag{18}$$

$V_p$ is defined here as $V_p = V_{spheroid}$, where $V_{spheroid}$ is the volume of the reconstructed oblate or prolate spheroid from planar images of the particle (Eq. (2), Sec. I.B). The density of the particle, then defined by:

$$\rho_p = \rho_i^{\text{bulk}} = \frac{m_p}{V_{spheroid}} \tag{19}$$

can be considered as an ice bulk density such that $\rho_i^{\text{bulk}} < \rho_i^{\text{core}}$. The values of $\Phi$ and $\Phi^{\perp}$ are computed from Eq. (2).

The ice-bulk density-based approach is therefore suitable when images are provided by the experiments allowing a spheroid geometrical reconstruction of the snowflake from a single planar view (Sec. I.B).

## III. Model validation using experimental data

The volume-based geometric models (H&L, Ga and H&S, Sec. II.B) are compared with the surface-based reference geometric model (H&W Sec. II.A) for the computation of the drag coefficient for snowflakes. Moreover, regarding the volume-based geometric models, the description of the snowflake by a dense particle (ice-core density-based approach, Sec. II.B.1) is compared to that by a less dense particle (ice-bulk density-based approach, Sec. II.B.2). The influence of the 2D to 3D reconstruction (oblate or prolate spheroid) is also studied in the case of the ice-bulk density-based description of the particle. This is summarized in Tab. 1 where the abbreviations used in the following are specified.

**Table 1 Abbreviations used for model comparison.**

| Type of geometric representation | Particle equivalent density (only for volume-based models) | Abbreviation | Ref. |
|---|---|---|---|
| Surface-based geometric model | | H&W | Sec. II.A |
| Volume-based geometric models | ice-core density-based ($\rho_p = \rho_i^{\text{core}}$) | H&L$^{\text{core}}$ | Sec. II.B, Eqs. (16) and (15) |
| | | Ga$^{\text{core}}$ | |
| | | H&S$^{\text{core}}$ | |
| | ice-bulk density-based ($\rho_p = \rho_i^{\text{bulk}}$) | H&L$^{\text{bulk}}$ | Sec. II.B, Eqs. (18) and (19) |
| | | Ga$^{\text{bulk}}$ | |
| | | H&S$^{\text{bulk}}$ | |

Terminal free fall velocities for 16 snowflakes are measured with the experimental method described in Sec. I.A. Conditions are described in row "Experiments" of Tab.2. For each of the studied drag models, the reconstructed geometrical parameters are also given for each of the three views (front, side and bottom). The averaged values of the parameters over the three views are noted *av*. The standard deviation is written *std*. Note that for each snowflake, the mass is measured experimentally (Sec. I.A). In this study, $m_p$ is therefore a known input for the models.

### A. Ice-bulk density-based description for volume-based geometric models

Figure 9 shows the comparison between the experimental ($\bar{v}_{p_\infty}^{exp}$, $X$ axis) and numerical ($\bar{v}_{p_\infty}^{num}$, $Y$ axis) results for the snowflake terminal velocity. The H&L$^{\text{bulk}}$, Ga$^{\text{bulk}}$ and H&S$^{\text{bulk}}$ models are compared with the H&W model (reference). The sensitivity to the 2D to 3D reconstruction is studied (oblate vs. prolate spheroid). Main diagonal (black solid line) means a perfect agreement. ± 30% relative error regions are shown (dashed lines). For the numerical solutions, each symbol in Fig. 9 is obtained by the arithmetic average (noted $\bar{v}_{p_\infty}^{num}$) of the three velocities computed from each of the three geometric reconstructions, which are themselves obtained from each of the three views (front, side, bottom). The three volume-based geometric models H&L$^{\text{bulk}}$, Ga$^{\text{bulk}}$ and H&S$^{\text{bulk}}$ are able to reproduce the terminal free fall velocity with an average relative accuracy of 30%, which is similar to that of the reference model H&W, except for the models H&L$^{\text{bulk}}$ and Ga$^{\text{bulk}}$ which tend to overestimate the snowflake fall velocity for some test cases, either for the prolate or oblate spheroid reconstruction. Generally speaking, the prolate or oblate spheroid reconstruction has a minor influence

**Table 2 Snowflake free fall study. 16 test cases. Experimental conditions and reconstructed geometric parameters**

| | N | | 1 | 2 | 3 | 4 | 5 | 6 | 7 | 8 | 9 | 10 | 11 | 12 | 13 | 14 | 15 | 16 |
|---|---|---|---|---|---|---|---|---|---|---|---|---|---|---|---|---|---|---|
| Experiments | Fall speed $v_{p_\infty}$ (m/s) | | 0.67 | 1.83 | 1.47 | 1.49 | 1.44 | 1.07 | 1.8 | 0.92 | 1.38 | 1.69 | 1.28 | 1.49 | 1.64 | 1.41 | 1.51 | 1.21 |
| | Mass $m_p$ (mg) | | 0.063 | 1.48 | 0.576 | 0.132 | 0.546 | 0.17 | 0.298 | 0.047 | 0.243 | 0.459 | 0.157 | 0.134 | 0.349 | 0.578 | 0.266 | 0.15 |
| (H&L, Ga, H&S)$^{\text{core}}$ | $d_m$ (mm) | | 0.51 | 1.46 | 1.06 | 0.65 | 1.04 | 0.71 | 0.85 | 0.46 | 0.8 | 0.98 | 0.69 | 0.65 | 0.9 | 1.06 | 0.82 | 0.68 |
| | $\rho_p$ (kg/m$^3$) | | 917.0 | 917.0 | 917.0 | 917.0 | 917.0 | 917.0 | 917.0 | 917.0 | 917.0 | 917.0 | 917.0 | 917.0 | 917.0 | 917.0 | 917.0 | 917.0 |
| (H&L, Ga, H&S)$^{\text{bulk}}$ (oblate reconstruction) | $d_V$ (mm) | front | 1.12 | 2.98 | 2.41 | 1.11 | 3.16 | 1.63 | 1.77 | 1.02 | 2.19 | 1.99 | 1.33 | 1.73 | 1.58 | 1.57 | 3.39 | 2.38 |
| | | side | 1.24 | 2.74 | 2.44 | 1.36 | 3.76 | 1.94 | 1.7 | 0.9 | 2.2 | 2.57 | 1.64 | 1.13 | 1.69 | 3.02 | 3.58 | 2.12 |
| | | bottom | 1.39 | 3.58 | 2.95 | 1.32 | 3.19 | 2.07 | 1.54 | 1.31 | 2.6 | 2.39 | 1.8 | 1.36 | 1.66 | 2.57 | 4.21 | 2.38 |
| | | av. | 1.25 | 3.1 | 2.6 | 1.26 | 3.37 | 1.88 | 1.67 | 1.08 | 2.33 | 2.32 | 1.59 | 1.41 | 1.64 | 2.39 | 3.73 | 2.3 |
| | | std. | 0.11 | 0.35 | 0.25 | 0.11 | 0.27 | 0.18 | 0.09 | 0.17 | 0.19 | 0.24 | 0.19 | 0.25 | 0.05 | 0.61 | 0.35 | 0.12 |
| | $\rho_b$ (kg/m$^3$) | front | 86.0 | 107.0 | 79.0 | 183.0 | 33.0 | 74.0 | 103.0 | 85.0 | 44.0 | 111.0 | 126.0 | 50.0 | 169.0 | 288.0 | 13.0 | 21.0 |
| | | side | 64.0 | 138.0 | 76.0 | 101.0 | 20.0 | 44.0 | 115.0 | 125.0 | 44.0 | 52.0 | 68.0 | 177.0 | 139.0 | 40.0 | 11.0 | 30.0 |
| | | bottom | 45.0 | 62.0 | 43.0 | 110.0 | 32.0 | 37.0 | 155.0 | 40.0 | 27.0 | 64.0 | 52.0 | 101.0 | 145.0 | 65.0 | 7.0 | 21.0 |
| | | av. | 65.0 | 102.0 | 66.0 | 131.0 | 28.0 | 52.0 | 124.0 | 83.0 | 38.0 | 76.0 | 82.0 | 109.0 | 151.0 | 131.0 | 10.0 | 24.0 |
| | | std. | 17.0 | 31.0 | 16.0 | 37.0 | 6.0 | 16.0 | 22.0 | 35.0 | 8.0 | 26.0 | 32.0 | 52.0 | 13.0 | 111.0 | 3.0 | 4.0 |
| | $\Phi$ (-) | front | 0.97 | 0.91 | 0.96 | 0.99 | 0.96 | 0.98 | 1.0 | 0.98 | 0.97 | 0.99 | 0.87 | 0.96 | 0.99 | 0.98 | 0.93 | 0.99 |
| | | side | 0.86 | 0.92 | 0.96 | 0.97 | 0.99 | 0.96 | 0.95 | 0.81 | 0.96 | 0.94 | 0.91 | 0.92 | 0.98 | 0.98 | 0.89 | 0.9 |
| | | bottom | 0.98 | 0.98 | 1.0 | 0.99 | 0.98 | 0.97 | 0.95 | 0.92 | 1.0 | 0.96 | 0.98 | 0.84 | 0.98 | 0.98 | 1.0 | 0.99 |
| | | av. | 0.93 | 0.93 | 0.97 | 0.98 | 0.98 | 0.97 | 0.97 | 0.9 | 0.98 | 0.96 | 0.92 | 0.91 | 0.98 | 0.98 | 0.94 | 0.96 |
| | | std. | 0.05 | 0.03 | 0.02 | 0.01 | 0.01 | 0.01 | 0.02 | 0.07 | 0.02 | 0.02 | 0.04 | 0.05 | 0.0 | 0.0 | 0.04 | 0.04 |
| | $\Phi^\perp$ (-) | front | 1.41 | 1.75 | 1.85 | 1.41 | 1.46 | 1.24 | 1.72 | 1.4 | 1.27 | 1.31 | 1.4 | 1.5 | 1.31 | 1.27 | 1.54 | 1.39 |
| | | side | 1.6 | 1.4 | 1.57 | 1.34 | 1.53 | 1.5 | 1.39 | 0.96 | 1.33 | 1.46 | 1.48 | 1.14 | 1.38 | 1.41 | 1.64 | 1.37 |
| | | bottom | 1.53 | 1.37 | 2.03 | 1.29 | 1.27 | 1.51 | 1.59 | 1.38 | 1.49 | 1.39 | 1.33 | 1.46 | 1.36 | 1.5 | 1.55 | 1.53 |
| | | av. | 1.51 | 1.51 | 1.82 | 1.35 | 1.42 | 1.42 | 1.56 | 1.25 | 1.37 | 1.39 | 1.4 | 1.37 | 1.35 | 1.39 | 1.58 | 1.43 |
| | | std. | 0.08 | 0.17 | 0.19 | 0.05 | 0.11 | 0.12 | 0.13 | 0.2 | 0.09 | 0.06 | 0.06 | 0.16 | 0.03 | 0.1 | 0.04 | 0.07 |
| (H&L, Ga, H&S)$^{\text{bulk}}$ (prolate reconstruction) | $d_V$ (mm) | front | 0.97 | 2.35 | 2.06 | 1.03 | 2.72 | 1.48 | 1.73 | 0.9 | 1.9 | 1.83 | 1.0 | 1.48 | 1.44 | 1.42 | 2.78 | 2.21 |
| | | side | 0.91 | 2.18 | 2.1 | 1.19 | 3.47 | 1.67 | 1.44 | 0.63 | 1.9 | 2.11 | 1.3 | 0.91 | 1.52 | 2.74 | 2.76 | 1.66 |
| | | bottom | 1.24 | 3.18 | 2.86 | 1.21 | 2.86 | 1.81 | 1.31 | 1.06 | 2.52 | 2.04 | 1.59 | 0.99 | 1.5 | 2.29 | 4.05 | 2.18 |
| | | av. | 1.04 | 2.57 | 2.34 | 1.14 | 3.02 | 1.65 | 1.49 | 0.86 | 2.11 | 1.99 | 1.3 | 1.13 | 1.49 | 2.15 | 3.19 | 2.02 |
| | | std. | 0.14 | 0.44 | 0.37 | 0.08 | 0.33 | 0.14 | 0.18 | 0.18 | 0.29 | 0.12 | 0.24 | 0.25 | 0.03 | 0.55 | 0.6 | 0.25 |
| | $\rho_b$ (kg/m$^3$) | front | 130.0 | 217.0 | 126.0 | 230.0 | 52.0 | 100.0 | 110.0 | 122.0 | 67.0 | 143.0 | 296.0 | 79.0 | 222.0 | 389.0 | 24.0 | 27.0 |
| | | side | 157.0 | 272.0 | 119.0 | 149.0 | 25.0 | 70.0 | 189.0 | 365.0 | 68.0 | 93.0 | 135.0 | 337.0 | 190.0 | 54.0 | 24.0 | 62.0 |
| | | bottom | 64.0 | 88.0 | 47.0 | 143.0 | 45.0 | 55.0 | 255.0 | 76.0 | 29.0 | 104.0 | 75.0 | 266.0 | 198.0 | 92.0 | 8.0 | 28.0 |
| | | av. | 117.0 | 192.0 | 97.0 | 174.0 | 40.0 | 75.0 | 185.0 | 188.0 | 55.0 | 113.0 | 168.0 | 227.0 | 203.0 | 178.0 | 19.0 | 39.0 |
| | | std. | 39.0 | 77.0 | 36.0 | 40.0 | 11.0 | 19.0 | 59.0 | 127.0 | 18.0 | 22.0 | 93.0 | 109.0 | 14.0 | 150.0 | 8.0 | 17.0 |
| | $\Phi$ (-) | front | 0.97 | 0.93 | 0.97 | 0.99 | 0.97 | 0.98 | 1.0 | 0.98 | 0.97 | 0.99 | 0.9 | 0.97 | 0.99 | 0.98 | 0.95 | 0.99 |
| | | side | 0.89 | 0.93 | 0.97 | 0.97 | 0.99 | 0.97 | 0.96 | 0.85 | 0.97 | 0.95 | 0.93 | 0.94 | 0.98 | 0.99 | 0.91 | 0.92 |
| | | bottom | 0.98 | 0.98 | 1.0 | 0.99 | 0.98 | 0.97 | 0.96 | 0.94 | 1.0 | 0.96 | 0.98 | 0.87 | 0.98 | 0.98 | 1.0 | 0.99 |
| | | av. | 0.95 | 0.95 | 0.98 | 0.98 | 0.98 | 0.98 | 0.97 | 0.92 | 0.98 | 0.97 | 0.94 | 0.93 | 0.98 | 0.98 | 0.95 | 0.97 |
| | | std. | 0.04 | 0.02 | 0.01 | 0.01 | 0.01 | 0.01 | 0.02 | 0.05 | 0.01 | 0.02 | 0.03 | 0.04 | 0.0 | 0.0 | 0.04 | 0.03 |
| | $\Phi^\perp$ (-) | front | 1.07 | 1.09 | 1.36 | 1.21 | 1.08 | 1.02 | 1.64 | 1.1 | 0.96 | 1.11 | 0.79 | 1.1 | 1.09 | 1.04 | 1.04 | 1.19 |
| | | side | 0.88 | 0.89 | 1.17 | 1.03 | 1.31 | 1.1 | 1.0 | 0.47 | 0.99 | 0.99 | 0.93 | 0.74 | 1.12 | 1.16 | 0.97 | 0.84 |
| | | bottom | 1.21 | 1.08 | 1.9 | 1.09 | 1.02 | 1.16 | 1.14 | 0.89 | 1.41 | 1.01 | 1.04 | 0.76 | 1.11 | 1.19 | 1.44 | 1.28 |
| | | av. | 1.05 | 1.02 | 1.47 | 1.11 | 1.14 | 1.09 | 1.26 | 0.82 | 1.12 | 1.04 | 0.92 | 0.87 | 1.1 | 1.13 | 1.15 | 1.1 |
| | | std. | 0.14 | 0.09 | 0.31 | 0.07 | 0.12 | 0.06 | 0.27 | 0.26 | 0.21 | 0.05 | 0.1 | 0.17 | 0.01 | 0.07 | 0.21 | 0.19 |
| H&W | $f_{max}$ (mm) | front | 1.29 | 3.78 | 2.81 | 1.2 | 3.67 | 1.81 | 1.81 | 1.15 | 2.53 | 2.17 | 1.77 | 2.01 | 1.73 | 1.73 | 4.14 | 2.57 |
| | | side | 1.67 | 3.43 | 2.83 | 1.55 | 4.06 | 2.26 | 2.01 | 1.28 | 2.55 | 3.11 | 2.07 | 1.4 | 1.87 | 3.32 | 4.65 | 2.71 |
| | | bottom | 1.56 | 4.02 | 3.05 | 1.44 | 3.56 | 2.36 | 1.82 | 1.62 | 2.67 | 2.81 | 2.03 | 1.88 | 1.85 | 2.89 | 4.38 | 2.6 |
| | | av. | 1.5 | 3.75 | 2.9 | 1.4 | 3.76 | 2.14 | 1.88 | 1.35 | 2.58 | 2.7 | 1.96 | 1.77 | 1.82 | 2.65 | 4.39 | 2.63 |
| | | std. | 0.16 | 0.24 | 0.11 | 0.15 | 0.21 | 0.24 | 0.09 | 0.2 | 0.06 | 0.4 | 0.13 | 0.26 | 0.06 | 0.67 | 0.21 | 0.06 |
| | $A_r$ (-) | front | 0.54 | 0.36 | 0.4 | 0.61 | 0.51 | 0.66 | 0.56 | 0.56 | 0.59 | 0.64 | 0.4 | 0.49 | 0.64 | 0.65 | 0.44 | 0.62 |
| | | side | 0.34 | 0.45 | 0.47 | 0.57 | 0.56 | 0.49 | 0.52 | 0.51 | 0.56 | 0.47 | 0.42 | 0.57 | 0.59 | 0.59 | 0.36 | 0.45 |
| | | bottom | 0.52 | 0.58 | 0.46 | 0.65 | 0.63 | 0.51 | 0.45 | 0.47 | 0.63 | 0.52 | 0.59 | 0.36 | 0.6 | 0.53 | 0.59 | 0.55 |
| | | av. | 0.47 | 0.46 | 0.44 | 0.61 | 0.57 | 0.55 | 0.51 | 0.51 | 0.59 | 0.54 | 0.47 | 0.47 | 0.61 | 0.59 | 0.46 | 0.54 |
| | | std. | 0.09 | 0.09 | 0.03 | 0.03 | 0.05 | 0.08 | 0.04 | 0.03 | 0.03 | 0.07 | 0.08 | 0.09 | 0.02 | 0.05 | 0.1 | 0.07 |

on the computation of the terminal velocity. The only point for which all models have a relative error greater than 30% is case 15 which is characterized by the lowest reconstructed bulk densities of the entire database.

For each of the models H&S$^{\text{bulk}}$, Ga$^{\text{bulk}}$, H&L$^{\text{bulk}}$ and H&W, and in addition to Fig. 9, Figs. 10 and 11 show error bars accounting for the snowflakes being described by three views (front, side and bottom, see Sec. I.A). The legend is similar to that of Fig. 9. The symbols showing $\bar{v}_{p_\infty}^{num}$ are reminded. The lengths of the error bars correspond to $\bar{v}_{p_\infty}^{num} \pm \sigma$ where $\sigma$ is the standard deviation calculated from $\bar{v}_{p_\infty}^{num}$ and the different velocities computed from the particles reconstructed from each of the three views. The error bar lengths indicate the dispersion of the computed free fall velocity with respect to the image chosen for the geometric reconstruction of the snowflake. Although the snowflakes were observed to have a privileged direction of fall in the experiments, the choice of the view direction for the oblate or prolate reconstruction has a limited effect on the model error, since the error bars are as a whole in the ± 30% relative error regions. This seems to be confirmed by the overall good behavior of the H&L model which does not depend on $\Phi^\perp$ and is therefore less sensitive to the view chosen to reconstruct the spheroid. For the 16 test cases, 31% of the best estimates for $\bar{v}_{p_\infty}^{num}$ are obtained with the front view, 28% with the bottom view, and 41% with the side view. This indicates that the models can be applied to estimate drag coefficients of snowflakes recorded from a random direction in airborne measurements.

Table 2 shows that the reconstructed densities $\rho_b$ vary from 5.0 kg.m$^{-3}$ to 389 kg.m$^{-3}$, far from the value of 917 kg.m$^{-3}$ used for ice particles in the framework of ice crystal icing. This is consistent with the observed complex shape of snowflakes as aggregates, which are poorly dense and contain air pockets.

Note that for the 16 test cases in Tab. 2, the range of values for the particle Reynolds number $Re_p$ varies from 44 to 362 for all the particles with the ice-bulk density-based description. This indicates that the drag force is driven by the intermediate law corresponding to a transition region between the Stokes' and Newton's regimes.

### B. Ice-core density-based description for volume-based geometric models

Figure 12 shows the comparison between the experimental $v_{p_\infty}^{exp}$ and numerical $v_{p_\infty}^{num}$ results for the snowflake terminal velocity. The H&L$^{\text{core}}$, Ga$^{\text{core}}$ and H&S$^{\text{core}}$ models are compared with the H&W model (reference). Main diagonal (black solid line) means a perfect agreement. ± 30% relative error regions are shown (dashed lines). Since there is no 2D to 3D reconstruction for the ice-core density-based description, the values of $\Phi$ and $\Phi^\perp$ for the models H&L$^{\text{core}}$, Ga$^{\text{core}}$ and H&S$^{\text{core}}$ cannot be deduced from the spheroid reconstruction as in the case of ice-bulk density-based models. The lack of particle geometric reconstruction from images also accounts for the missing error bars in Fig. 12. To determine $\Phi$ and $\Phi^\perp$, an error minimization procedure is performed on all 16 flakes and for each model between the experimental and numerically computed terminal free fall velocities. Indeed, contrary to ice crystals where $\Phi = 1$ and $\Phi^\perp = 1$ lead to acceptable predictions of the particle trajectories and in particular of the collection efficiency [19, 22], such an assumption is no longer acceptable for the case of aggregates where the geometry is more complex and the

inertia is lower. The mapping of the $L_2$-norm error as a function of $\Phi$ and $\Phi^{\perp}$ is shown in Fig. 13 for each model. The vertical lines in Fig. 13a simply mean that the H&L model does not depend on $\Phi^{\perp}$. The values of $\Phi$ and $\Phi^{\perp}$ that minimize the $L_2$-error are those used in Fig. 12. The optimal values obtained for $\Phi$ and $\Phi^{\perp}$ are below 0.4, at levels much smaller than those used in the framework of ice crystal icing where $\Phi$ and $\Phi^{\perp}$ were chosen between 0.8 and 1 [19, 22]. Thus, provided that the geometric complexity of the snowflake is taken into account by adapting $\Phi$ and $\Phi^{\perp}$, the description of the snowflake by a dense particle allows the simulation of terminal free fall velocity with an accuracy comparable to the previous method where the snowflake is modeled by a less dense spheroid particle.

For the 16 test cases in Tab. 2, the range of values for the particle Reynolds number $Re_p$ varies from 22 to 170 for all the particles with the ice-core density-based description. As expected, the values for $Re_p$ are lower than for the ice-bulk density-based approach. However, the observed regimes for the drag force are similar, namely the intermediate law between the Stokes' and Newton's regimes.

## IV. Discussion

Surface-based and volume-based geometric models provide comparable accuracy for computing the terminal free fall velocity of snowflakes. This validates the extension to snowy conditions of the volume-based geometric models initially developed for ice crystal icing. Among the volume-based models, the ice-bulk and ice-core density-based descriptions are fairly similar in the sense that they assign a different relative weight to $C_D$ and $A_{ref}$, keeping in mind that only the product $C_D \cdot A_{ref}$ is relevant for the computation of the drag force (Eq. (3)). For the ice-bulk density-based approach, the snowflake is represented by a particle of regular shape and low bulk density, taking into account air gaps inside the particle. This leads to a higher value for $A_{ref}$ and in return a lower value for $C_D$. On the contrary, for the ice-core density-based approach, the characteristic size of the particle $d_{ref}$ is arbitrarily defined as the equivalent mass diameter thus leading to a smaller value for $A_{ref}$ and a in turn to a higher value for $C_D$ (resulting from smaller values of $\Phi$ and $\Phi_{\perp}$). However, even if both approaches ultimately lead to results of comparable accuracy, the ice-bulk density-based approach is more physically satisfactory since it takes into account (in a simplified way) the geometry of the particle and thus does not require the use of adjustable parameters ($\Phi$ and $\Phi^{\perp}$) whose optimal values obtained in the case of this study are not intended to be general.

The preferred use between the ice-bulk or the ice-core density-based geometric reconstruction for the snowflake depends on the type of input data available to describe the particle. If an image of the snowflake is provided, then the ice-bulk density-based approach is to be preferred since all the geometric characteristics of the particle can be deduced from the 3D spheroid reconstruction. If such an image is not available, then the ice-core density-based approach can provide an interesting alternative. All that is needed is then the mass distribution of the particles in the cloud and as well the corresponding distributions for the particle sphericities (and orthogonal sphericities for the Ga and H&S drag models). The need to provide sphericity is clearly the weak point of this second approach. A parametric study in the

spirit of the present study would be necessary to provide sphericity values for different types of particles that may be encountered in a cloud.

Regarding the accuracy of the geometric reconstruction of the snowflake, Leinonen *et al.* [34] proposed a 3D reconstruction from a triplet of images and an artificial intelligence algorithm based on Generative Adversarial Network (GAN) to reconstruct the mass and geometric descriptors of the particle. Future work should propose new drag models with more input data adapted to the improved accuracy of the geometric reconstruction.

## Conclusions

In this paper, a comparison is presented between different empirical approaches to estimate the drag force of a snowflake when incomplete information on its shape is available. In this case, it is necessary to use simple geometrical descriptors in order to compute the reference surface $A_{ref}$ of the particle and its drag coefficient $C_D$, knowing that only the product is relevant for the drag force. The conclusion of the present study, based on the analysis of an experimental database containing 16 snowflakes of various shapes and sizes, is that the different approaches are globally equivalent in terms of relative error on the terminal free fall velocity of the snowflakes. However, the ice-bulk density-based approach seems more satisfactory because there is a simple procedure to determine the geometric parameters ($d_V$, $\Phi$ and $\Phi^{\perp}$) from a single 2D image of the particle. Determining $\Phi$ and $\Phi^{\perp}$ is more problematic in the case of the ice-core density-based approach since these parameters are difficult to be estimated *a priori* for very irregular particles and should rather be considered as adjustable parameters for the computation of the drag coefficient. It remains questionable whether the values of the order of 0.2 to 0.4 found in the present work can be applied to a large class of snowflakes. It is however confirmed [29] that they are far too low for more regular particles such as ice crystals.

The level of confidence in the snowflake mass estimate has not been discussed in this work since it is known experimentally. In reality, the estimation of the particle mass is often provided by correlative mass-diameter relations [8] which are sources of additional inaccuracies. Thus, to improve the prediction of snowflake trajectories, joint efforts will have to be made in the geometrical description of the particles, the estimation of their mass, and the accuracy of the drag coefficient model.

In the context of future developments of heat exchange models for snow particles, the validity of the volume-based geometric models to describe the dynamics of snowflakes is an argument in favor of extending the thermal models initially proposed for ice crystals to snow particles. The latter are actually derived from a Reynolds-type analogy between heat transfer and momentum where drag forces are computed with the H&S model for the drag coefficient $C_D$ [29].

## Appendix

A summary of the drag models $C_D^{H\&L}$, $C_D^{Ga}$ and $C_D^{H\&S}$ is provided here.

- For the Haider & Levenspiel (H&L) model [30], the drag coefficient is given by:

$$C_D^{H\&L} = \frac{24}{Re_p}\left(1 + aRe_p^b\right) + \frac{c}{1 + dRe_p^{-1}} \tag{20}$$

where the coefficients $a$, $b$, $c$ and $d$ are given by:

$$a = \exp\left(2.3288 - 6.4581\Phi + 2.4486\Phi^2\right) \tag{21a}$$

$$b = 0.0964 + 0.5565\Phi \tag{21b}$$

$$c = \exp\left(4.905 - 13.8944\Phi + 18.4222\Phi^2 - 10.2599\Phi^3\right) \tag{21c}$$

$$d = \exp\left(1.4681 + 12.2584\Phi - 20.7322\Phi^2 + 15.8855\Phi^3\right) \tag{21d}$$

- For the Ganser (Ga) model [31], the drag coefficient is given by:

$$C_D^{Ga} = C_{shape} \cdot C_D^{Ga,\star} \tag{22}$$

where $C_D^{Ga,\star}$ is defined as:

$$C_D^{Ga,\star} = \frac{24}{Re_p^\star}\left(1 + 0.1118\left(Re_p^\star\right)^{0.6567}\right) + \frac{0.4305}{1 + 3305\left(Re_p^\star\right)^{-1}} \tag{23}$$

$Re_p^\star$ is written as a function of the particle Reynolds number $Re_p$ as follows:

$$Re_p^\star = \frac{C_{shape} Re_p}{f_{shape}} \tag{24}$$

In Eqs. (22) and (24), $C_{shape}$ and $f_{shape}$ are defined as:

$$C_{shape} = 10^{a[-\log(\Phi)]^b} \tag{25a}$$

$$f_{shape} = \frac{2}{3}\Phi^{-1/2} + \frac{1}{3}\left(\Phi^\perp\right)^{-1/2} \tag{25b}$$

- For the Hölzer & Sommerfeld (H&S) model [32], the drag coefficient is given by:

$$C_D^{H\&S} = \frac{8}{Re_p}\left(\Phi^\perp\right)^{-1/2} + \frac{16}{Re_p}\Phi^{-1/2} + \frac{3}{Re_p^{1/2}}\Phi^{-3/4} + \frac{0.42}{\Phi^\perp}10^{0.4[-\log(\Phi)]^{0.2}} \tag{26}$$

## Acknowledgments

The funding from the European Union's Horizon 2020 research and innovation program under grant agreement No 824310 is gratefully acknowledged. The authors also gratefully acknowledge Pierre Coutris from CNRS (French National Center for Scientific Research) for the picture of the CIP, HSI and PIP probes (Fig. 2).

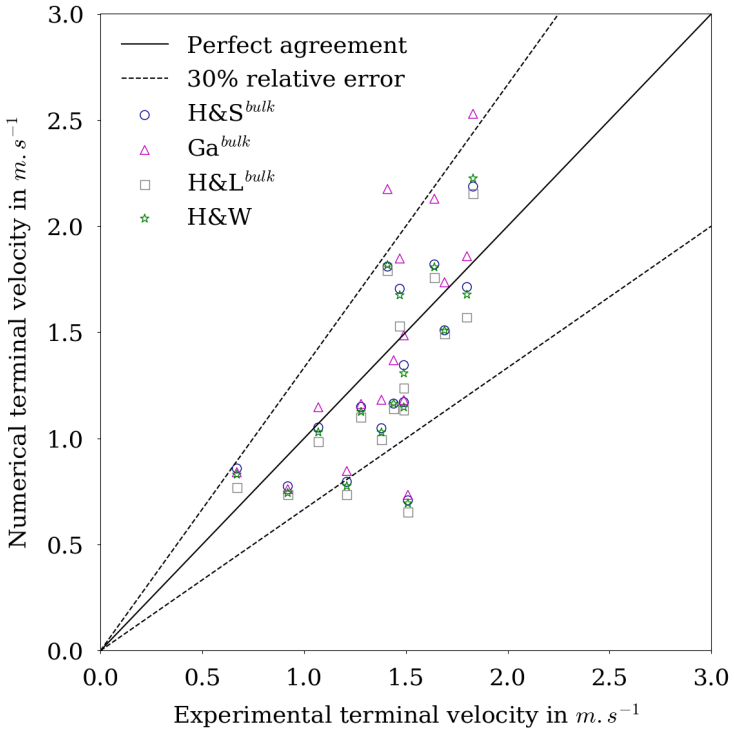


(a) Oblate spheroid reconstruction.

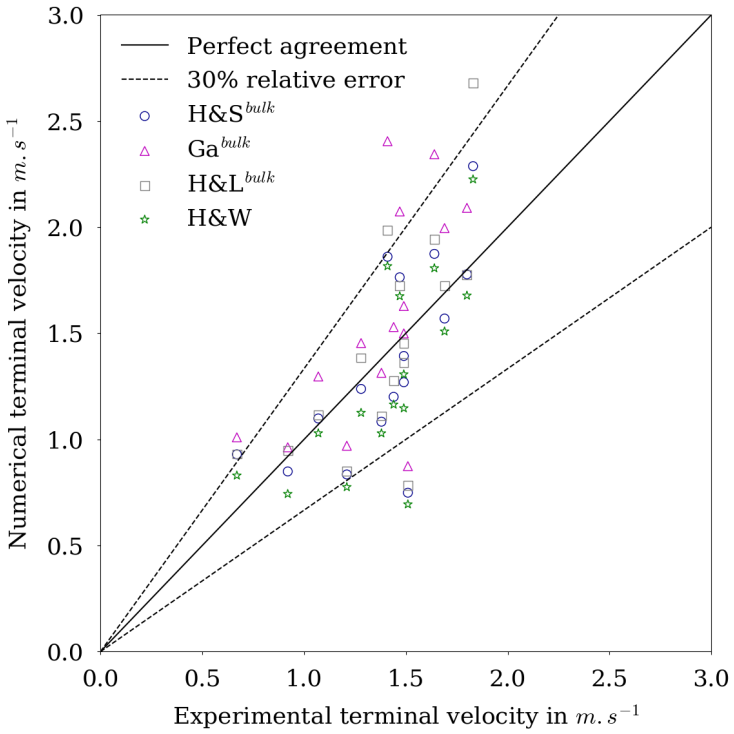


(b) Prolate spheroid reconstruction.

**Fig. 9 Average numerical velocity ($\bar{v}_{p_\infty}^{num}$) vs. experimental velocity ($v_{p_\infty}^{exp}$). Ice-bulk density-based reconstructions (H&L$^{\mathbf{bulk}}$, Ga$^{\mathbf{bulk}}$ and H&S$^{\mathbf{bulk}}$) vs. H&W model (reference).**

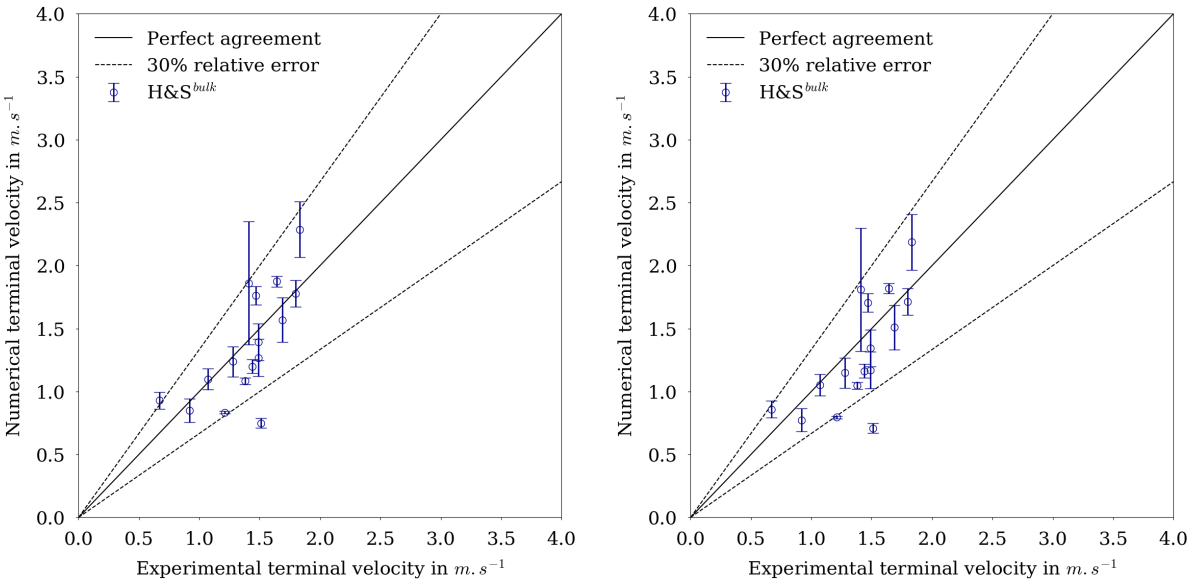


(a) H&S$^{\text{bulk}}$, prolate.




(b) H&S$^{\text{bulk}}$, oblate.

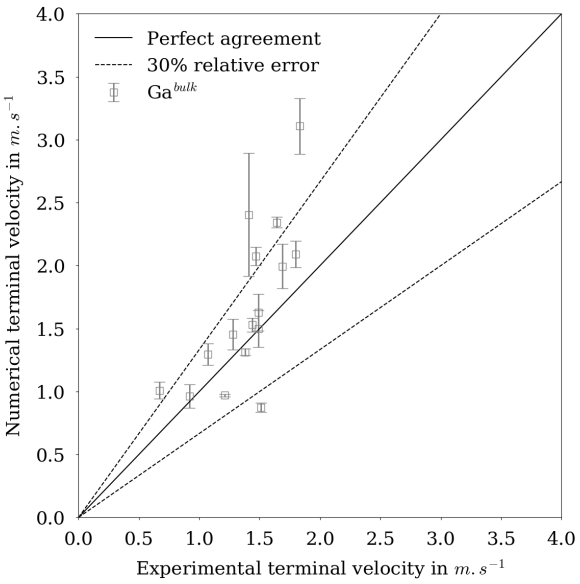


(c) Ga$^{\text{bulk}}$, prolate.

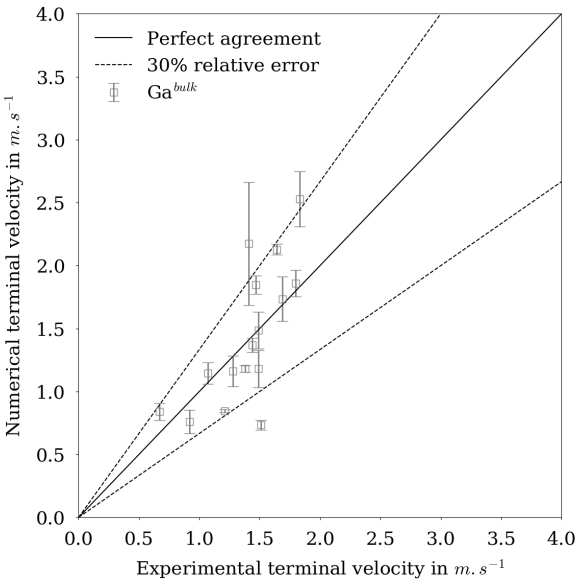


(d) Ga$^{\text{bulk}}$, oblate.

**Fig. 10 $v_{p_\infty}^{num}$ vs. $v_{p_\infty}^{exp}$. Dispersion of $v_{p_\infty}^{num}$ around $\bar{v}_{p_\infty}^{num}$ and influence of the chosen view for the reconstructed geometry. H&S$^{\text{bulk}}$ and Ga$^{\text{bulk}}$ models.**

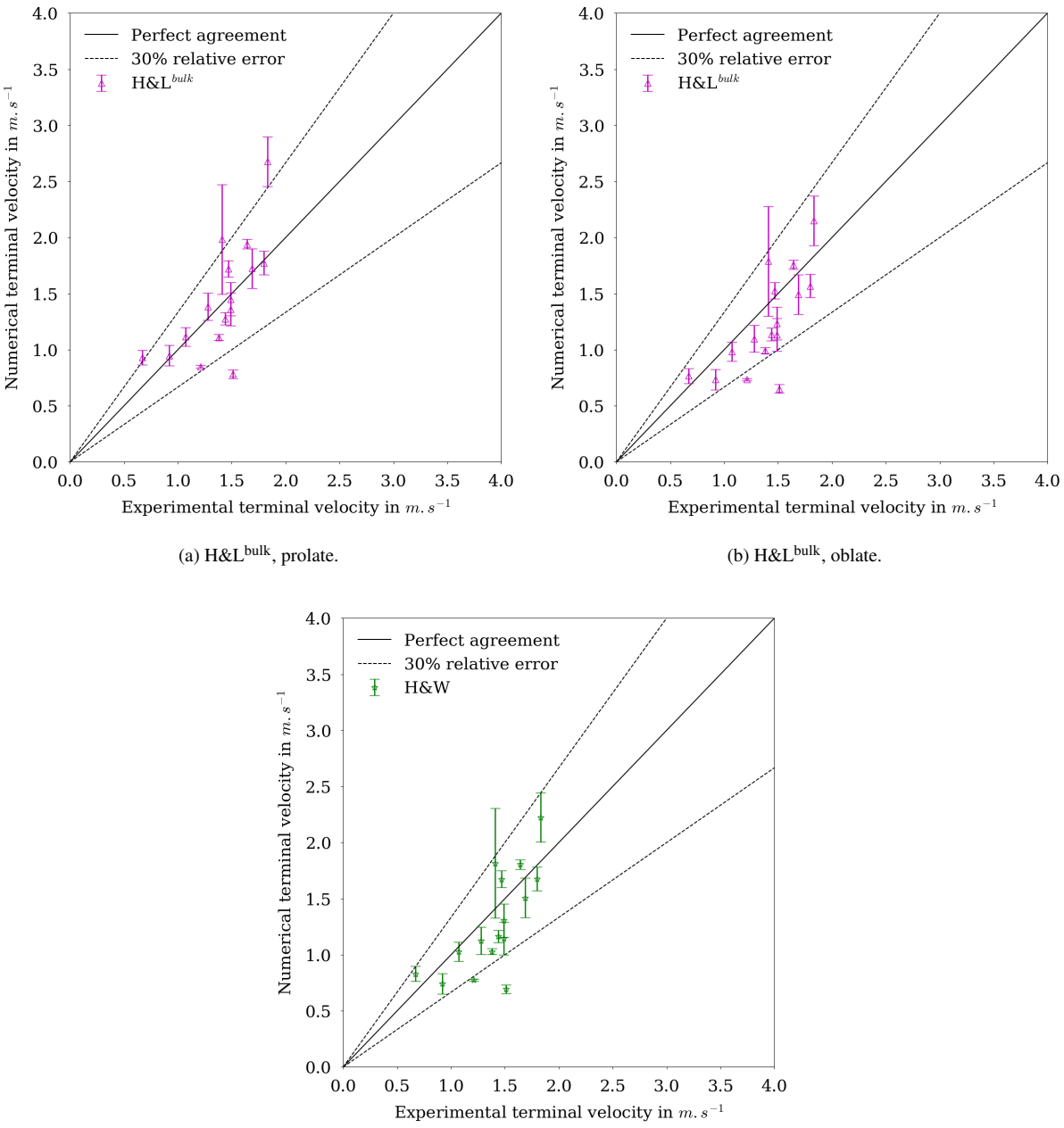


(a) H&L$^{\text{bulk}}$, prolate.

(b) H&L$^{\text{bulk}}$, oblate.

(c) H&W.

**Fig. 11 $v_{p_\infty}^{num}$ vs. $v_{p_\infty}^{exp}$. Dispersion of $v_{p_\infty}^{num}$ around $\bar{v}_{p_\infty}^{num}$ and influence of the chosen view for the reconstructed geometry. H&L$^{\text{bulk}}$ and H&W models.**

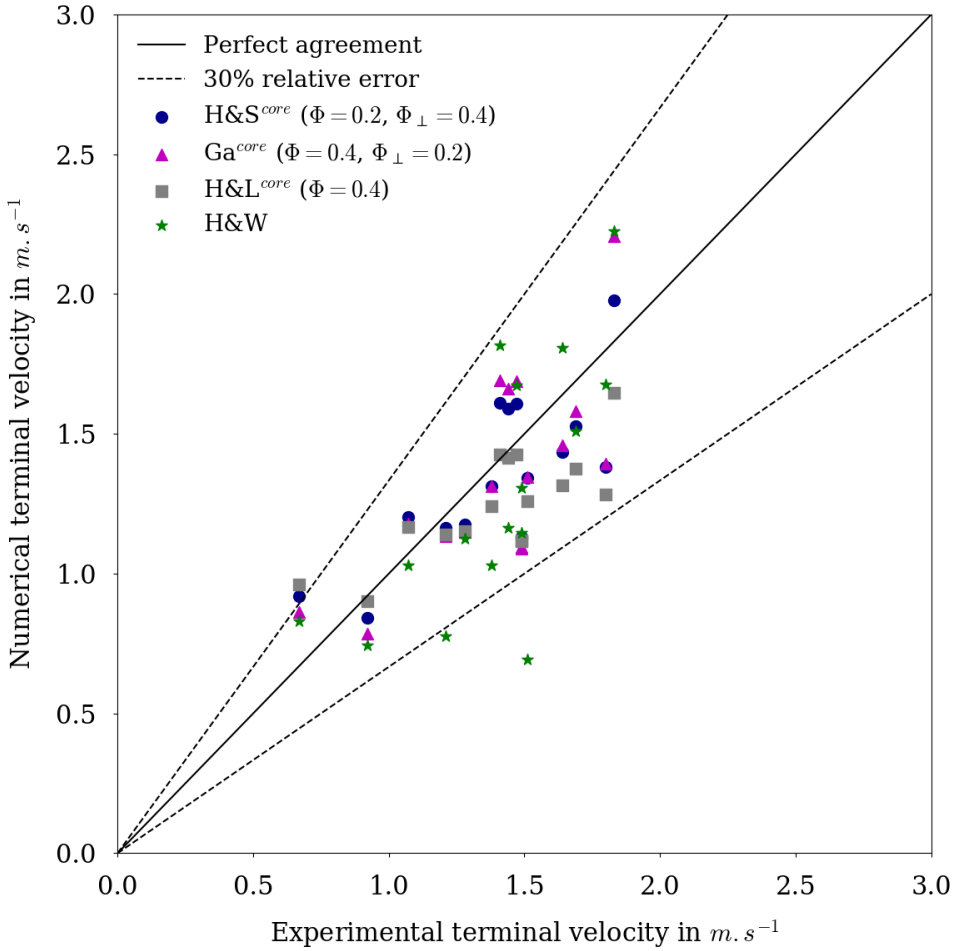


**Fig. 12 Numerical velocity ($v_{p_\infty}^{num}$) vs. experimental velocity ($v_{p_\infty}^{exp}$). Ice-core density-based reconstructions (H&L$^{core}$, Ga$^{core}$ and H&S$^{core}$) vs. H&W model (reference).**

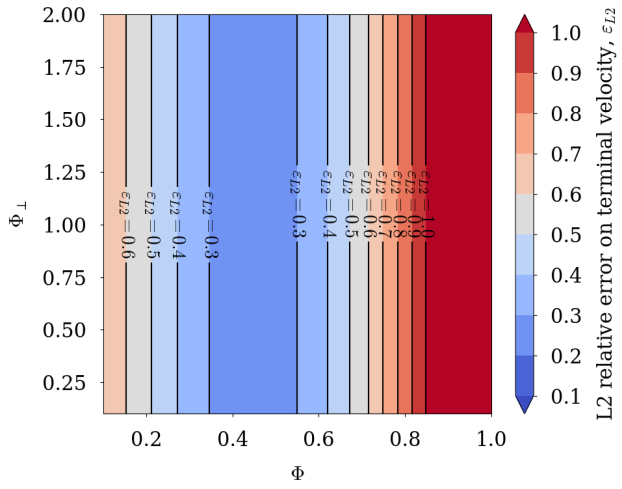


(a) H&L$^{\text{core}}$

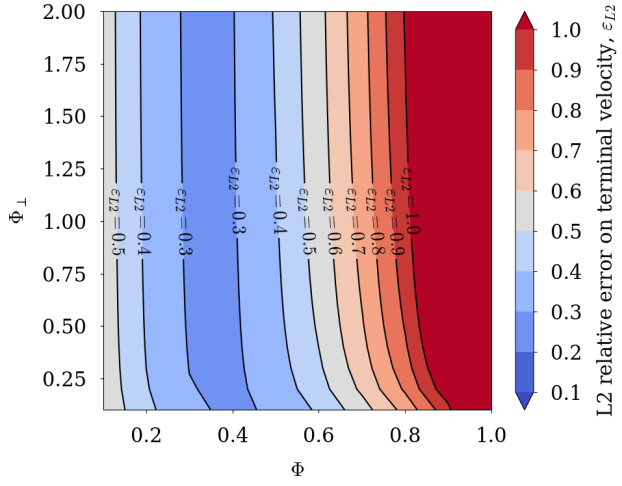


(b) Ga$^{\text{core}}$

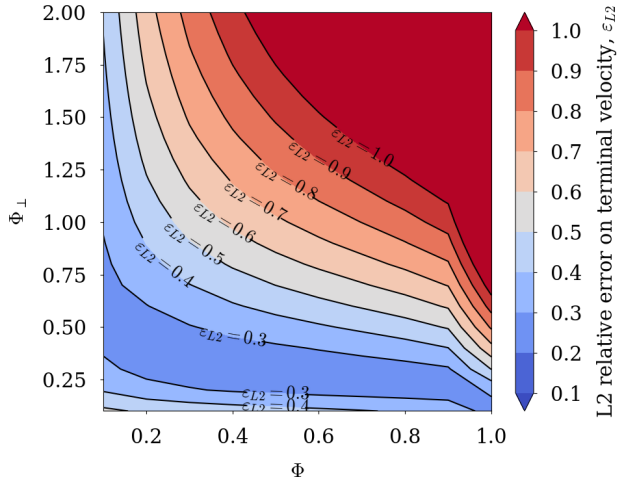


(c) H&S$^{\text{core}}$

**Fig. 13** $L_2$**-error between** $v_{p_\infty}^{num}$ **and** $v_{p_\infty}^{exp}$ **(all snowflakes). Influence of** $\Phi$ **and** $\Phi^{\perp}$ **on the ice-core density-based description.**

## References


[1] Nakaya, U., and Terada, T., "Simultaneous observations of the mass, falling velocity and form of individual snow crystals," *Journal of the Faculty of Science, Hokkaido Imperial University*, Vol. 1, No. 7, 1935, pp. 191–200. URL http://hdl.handle.net/2115/34452.

[2] Heymsfield, A. J., and Westbrook, C., "Advances in the estimation of ice particle fall speeds using laboratory and field measurements," *Journal of the Atmospheric Sciences*, Vol. 67, No. 8, 2010, pp. 2469–2482. https://doi.org/10.1175/2010JAS3379.1.

[3] Heymsfield, A. J., and Kajikawa, M., "An improved approach to calculating terminal velocities of plate-like crystals and graupel," *Journal of the atmospheric sciences*, Vol. 44, No. 7, 1987, pp. 1088–1099. https://doi.org/10.1175/1520-0469(1987)044<1088:AIATCT>2.0.CO;2.

[4] Khvorostyanov, V. I., and Curry, J. A., "Terminal velocities of droplets and crystals: Power laws with continuous parameters over the size spectrum," *Journal of the atmospheric sciences*, Vol. 59, No. 11, 2002, pp. 1872–1884. https://doi.org/10.1175/1520-0469(2002)059<1872:TVODAC>2.0.CO;2.

[5] Khvorostyanov, V. I., and Curry, J. A., "Fall velocities of hydrometeors in the atmosphere: Refinements to a continuous analytical power law," *Journal of the atmospheric sciences*, Vol. 62, No. 12, 2005, pp. 4343–4357. https://doi.org/10.1175/JAS3622.1.

[6] Mitchell, D. L., "Use of mass-and area-dimensional power laws for determining precipitation particle terminal velocities," *Journal of the atmospheric sciences*, Vol. 53, No. 12, 1996, pp. 1710–1723. https://doi.org/10.1175/1520-0469(1996)053<1710:UOMAAD>2.0.CO;2.

[7] Mitchell, W. F., and Tiesinga, E., "Adaptive grid refinement for a model of two confined and interacting atoms," *Applied numerical mathematics*, Vol. 52, No. 2-3, 2005, pp. 235–250. https://doi.org/10.1016/j.apnum.2004.08.034.

[8] Pruppacher, H. R., and Klett, J. D., *Microphysics of Clouds and Precipitation: Reprinted 1980*, Springer Science & Business Media, 2012. https://doi.org/10.1007/978-0-306-48100-0.

[9] Garrett, T., Fallgatter, C., Shkurko, K., and Howlett, D., "Fall speed measurement and high-resolution multi-angle photography of hydrometeors in free fall," *Atmospheric Measurement Techniques*, Vol. 5, No. 11, 2012, pp. 2625–2633. https://doi.org/10.5194/amt-5-2625-2012.

[10] "ICE GENESIS (Creating the nExt GENEration of 3D SImulation meanS for icing), project overview." https://www.ice-genesis.eu/media/articles/files/Workshop_presentations/ICE_GENESIS_project_overview.pdf, Jan. 2019.

[11] Dezitter, F., Grandin, A., Brenguier, J.-L., Hervy, F., Schlager, H., Villedieu, P., and Zalamansky, G., "HAIC-High Altitude Ice Crystals," *5th AIAA Atmospheric and Space Environments Conference, AIAA-2013-2674, San Diego, USA*, 24-27 June 2013. https://doi.org/10.2514/6.2013-2674.

[12] Villedieu, P., Trontin, P., Aouizerate, G., Bansmer, S., Vanacore, P., Roisman, I., and Tropea, C., "MUSIC-haic (MUltidisciplinary tools for the Simulation of In-flight iCing due to High Altitude Ice Crystals): 3D multidisciplinary tools for the simulation of in-flight icing due to high altitude ice crystals." *SAE (Society of Automotive Engineers) International Journal of Advances and Current Practices in Mobility*, Vol. 2, No. 1, 2020, pp. 78–89. https://doi.org/10.4271/2019-01-1962.

[13] Loth, E., "Drag of non-spherical solid particles of regular and irregular shape," *Powder Technology*, Vol. 182, No. 3, 2008, pp. 342–353. https://doi.org/10.1016/j.powtec.2007.06.001.

[14] Hauk, T., "Investigation of the Impact and Melting Process of Ice Particles," Ph.D. thesis, T.U. Darmstadt, 2016. URL `https://tuprints.ulb.tu-darmstadt.de/id/eprint/5280`.

[15] Kintea, D., "Hydrodynamics and Thermodynamics of Ice Particle Accretion," Ph.D. thesis, T.U. Darmstadt, 2016. URL `https://tuprints.ulb.tu-darmstadt.de/id/eprint/5452`.

[16] Baumert, A., "Experimental and numerical studies on ice crystal icing of civil aircraft," Ph.D. thesis, T.U. Braunschweig, 2019.

[17] Hauk, T., Bonaccurso, E., Villedieu, P., and Trontin, P., "Theoretical and Experimental Investigation of the Melting Process of Ice Particles," *Journal of Thermophysics and Heat Transfer*, Vol. 30, No. 4, 2016, pp. 946–954. https://doi.org/10.2514/1.T4886.

[18] Kintea, D., Hauk, T., Roisman, I., and Tropea, C., "Shape evolution of a melting nonspherical particle," *Physical Review E*, Vol. 92, No. 3, 2015, p. 033012. https://doi.org/10.1103/PhysRevE.92.033012.

[19] Baumert, A., Bansmer, S., Trontin, P., and Villedieu, P., "Experimental and numerical investigations on aircraft icing at mixed phase conditions," *International Journal of Heat and Mass Transfer*, Vol. 123, 2018, pp. 957–978. https://doi.org/10.1016/j.ijheatmasstransfer.2018.02.008.

[20] Villedieu, P., Trontin, P., and Chauvin, R., "A comprehensive numerical model for mixed-phase and glaciated icing conditions," *8th AIAA Atmospheric and Space Environments Conference, AIAA 2016-3742, Washington, D.C., USA.*, 13-17 June 2016. https://doi.org/10.2514/6.2016-3742.

[21] Aouizerate, G., Charton, V., Balland, M., Senoner, J., Trontin, P., Laurent, C., Blanchard, G., and Villedieu, P., "Ice crystals trajectory calculations in a turbofan engine." *2018 Atmospheric and Space Environments Conference, AIAA-2018-4130, Atlanta, USA*, 25-29 June 2018. https://doi.org/10.2514/6.2018-4130.

[22] Trontin, P., and Villedieu, P., "A comprehensive accretion model for glaciated icing conditions," *International Journal of Multiphase Flow.*, Vol. 108, 2018, pp. 105–123. https://doi.org/10.1016/j.ijmultiphaseflow.2018.06.023.

[23] Norde, E., Senoner, J., van der Weide, E., Trontin, P., Hoeijmakers, H., and Villedieu, P., "Eulerian and Lagrangian Ice Crystal Trajectory Simulations in a Generic Turbofan Compressor," *Journal of Propulsion and Power*, Vol. 35, No. 1, 2019, pp. 26–40. https://doi.org/10.2514/1.B36916.

[24] Hauk, T., Bonaccurso, E., Roisman, I., and Tropea, C., "Ice crystal impact onto a dry solid wall. Particle fragmentation," *Proceedings of the Royal Society A*, Vol. 471, No. 2181, 2015, p. 20150399. https://doi.org/10.1098/rspa.2015.0399.

[25] Roisman, I., and Tropea, C., "Impact of a crushing ice particle onto a dry solid wall," *Proceedings of the Royal Society A*, Vol. 471, No. 2183, 2015, p. 20150525. https://doi.org/10.1098/rspa.2015.0525.

[26] Kintea, D., Breitenbach, J., Thammanna Gurumurthy, V., Roisman, I., and Tropea, C., "On the influence of surface tension during the impact of particles on a liquid-gaseous interface," *Physics of Fluids*, Vol. 28, No. 1, 2016, p. 012108. https://doi.org/10.1063/1.4939285.

[27] Kintea, D., Roisman, I., and Tropea, C., "Transport processes in a wet granular ice layer: Model for ice accretion and shedding," *International Journal of Heat and Mass Transfer*, Vol. 97, 2016, pp. 461–472. https://doi.org/10.1016/j.ijheatmasstransfer.2016.01.076.

[28] Kintea, D., Schremb, M., Roisman, I., and Tropea, C., "Numerical investigation of ice particle accretion on heated surfaces with application to aircraft engines," *11th AIAA/ASME (American Society of Mechanical Engineers) Joint Thermophysics and Heat Transfer Conference, AIAA-2014-2820, Atlanta, USA*, 16-20 June 2014. https://doi.org/10.2514/6.2014-2820.

[29] Villedieu, P., Trontin, P., and Chauvin, R., "Glaciated and mixed phase ice accretion modeling using ONERA (Office National d'Etudes et de Recherches Aérospatiales) 2D icing suite," *6th AIAA atmospheric and space environments conference, AIAA 2014-2199, Atlanta, USA*, 16-20 June 2014. https://doi.org/10.2514/6.2014-2199.

[30] Haider, A., and Levenspiel, O., "Drag coefficient and terminal velocity of spherical and nonspherical particles," *Powder technology*, Vol. 58, No. 1, 1989, pp. 63–70. https://doi.org/10.1016/0032-5910(89)80008-7.

[31] Ganser, G. H., "A rational approach to drag prediction of spherical and nonspherical particles," *Powder technology*, Vol. 77, No. 2, 1993, pp. 143–152. https://doi.org/10.1016/0032-5910(93)80051-B.

[32] Hölzer, A., and Sommerfeld, M., "New simple correlation formula for the drag coefficient of non-spherical particles," *Powder Technology*, Vol. 184, No. 3, 2008, pp. 361–365. https://doi.org/10.1016/j.powtec.2007.08.021.

[33] Abraham, F. F., "Functional dependence of drag coefficient of a sphere on Reynolds number," *The Physics of Fluids*, Vol. 13, No. 8, 1970, pp. 2194–2195. https://doi.org/10.1063/1.1693218.

[34] Leinonen, J., Grazioli, J., and Berne, A., "Reconstruction of the mass and geometry of snowfall particles from Multi-Angle Snowflake Camera (MASC) images," *Atmospheric Measurement Techniques*, Vol. 14, No. 10, 2021, pp. 6851–6866. https://doi.org/10.5194/amt-14-6851-2021.